

# From macro to micro: multi-scale study of plasmonic nanocoating self-assembled on multijunction bulk solar cells

Dan Su

Southeast University

Xiao-Yang Zhang

Southeast University

Lei Lv

Southeast University

Huan-Li Zhou

Southeast University

Shan-Jiang Wang

Southeast University

Yi Yang

Southeast University

Jing-Yuan Wu

Donghua University

Ning Zhao

Southeast University

Tong Zhang (✉ [tzhang@seu.edu.cn](mailto:tzhang@seu.edu.cn))

Southeast University

---

## Article

**Keywords:** Ag@SiO<sub>2</sub> core-shell nanostructures, Self-assembly method, Multijunction solar cell, Submicrometer-scale photoelectrical response

**Posted Date:** November 13th, 2020

**DOI:** <https://doi.org/10.21203/rs.3.rs-105732/v1>

**License:**  This work is licensed under a Creative Commons Attribution 4.0 International License.

[Read Full License](#)

---

# **From macro to micro: multi-scale study of plasmonic nanocoating self-assembled on multijunction bulk solar cells**

Dan Su<sup>1,&</sup>, Xiao-Yang Zhang<sup>2,3,&</sup>, Lei Lv<sup>2</sup>, Huan-Li Zhou<sup>2</sup>, Shan-Jiang Wang<sup>2</sup>, Yi Yang<sup>2</sup>, Jing-Yuan Wu<sup>4</sup>, Ning Zhao<sup>1,2,3</sup>, Tong Zhang<sup>1,2,3,\*</sup>

1. Key Laboratory of Micro-Inertial Instrument and Advanced Navigation Technology, Ministry of Education, School of Instrument Science and Engineering, Southeast University, Nanjing, 210096, People's Republic of China

2. Joint International Research Laboratory of Information Display and Visualization, School of Electronic Science and Engineering, Southeast University, Nanjing, 210096, People's Republic of China.

3. Suzhou Key Laboratory of Metal Nano-Optoelectronic Technology, Southeast University Suzhou Campus, Suzhou, 215123, People's Republic of China

4. Photonics Laboratory and Institute of Functional Materials, College of Science, Donghua University, Shanghai, 201620, People's Republic of China

& These authors contributed equally to this work and should be considered co-first authors

\* Corresponding author, E-mail: tzhang@seu.edu.cn

Nanophotonics pours into new opportunities to achieve ultrahigh-efficiency solar cells, attracting tremendous interests from photovoltaic research and industry. Plasmonic nanostructures, enabling strong light-matter interaction at the nanoscale, have been widely used for efficiency enhancement in thin-film solar cell devices based on plasmonic near-field effects. Unlike thin-film device cases, we found forward scattering and inter-particle coupling engineering of subwavelength plasmonic nanostructures are the key to enhance the efficiency of bulk multijunction solar cells (MJSCs). As a proof of concept, we studied the plasmonic enhancement of Ag@SiO<sub>2</sub> nanocoating self-assembled on InGaP/GaInAs/Ge MJSCs at both macro and micro scales. From the macro measurements, the experimental enhancement of Ag@SiO<sub>2</sub> core-shell nanostructure could be well-matched with the simulational results, where strong forward scattering and suppressed interparticle coupling could be simultaneously achieved by employing ~ 22 nm SiO<sub>2</sub> shell layer. Using a double excitation method under an infinity optical microscope, we directly observed multi-wavelength uniform photocurrent enhancements on MJSCs at a submicrometer scale. This study will provide an effective strategy and opening up new opportunities to explore high-efficient MJSCs using nanophotonics.

**Key words:** Ag@SiO<sub>2</sub> core-shell nanostructures; Self-assembly method; Multijunction solar cell; Submicrometer-scale photoelectrical response

Nanophotonics is believed to have great potential in realizing ultrahigh-efficiency solar cells, which arouses attention both from academia and industry interest<sup>1</sup>. With the capability to interact with photons strongly at the subwavelength scale, plasmonic nanostructures (such as Au, Ag nanoparticles) have been widely applied to enhance thin-film solar cells<sup>2-5</sup>. Different physical explanations are proposed, including localized light concentration, scattering into the active layer, scattering into guided modes, plasmonic hot-electron effects, plasmon resonant energy transfer, or synergistic effects<sup>4,6-12</sup>. Among other things, the primary consideration in thin-film solar cells is to make full use of the near-field effects<sup>7,8,11,13,14</sup>. MJSCs, consisting of two or more stacked junctions of semiconductors in series connection, have been verified as a viable approach to converting wide-spectral solar energy efficiently into electricity and hold the record for the highest solar conversion efficiency<sup>15</sup>. When integrating plasmonic structures with the bulk MJSCs, the interaction between nanostructures and solar cells shows some features different from thin-film solar cells. First, the active layer of MJSC is too thick to put into the subwavelength near-field region of plasmonic nanostructures. Besides, the parasitic absorption and directional scattering of nanostructures should be carefully considered since the bulk solar cells already convert the photons into electrons with high efficiency<sup>16</sup>. It has been demonstrated that Ag and Au nanostructures are difficult to enhance the efficiency of the bulk solar cell due to their absorption losses in the visible region according to the previously reported results<sup>16-18</sup>. One potential strategy is to reduce plasmonic absorption losses using Al nanostructures with lower absorption in the visible range, which was demonstrated useful in specific circumstances through numerical simulation<sup>16</sup>. Another potential strategy is to enhance the forward scattering of plasmonic nanostructures on MJSCs, which has not been studied to the best of our knowledge.

Compared to metallic nanostructures, metal-dielectric composite nanostructures provide more versatile control over optical, electronic, and chemical properties<sup>13,19,20</sup>. For example, a thin-layer shell may reduce nanoparticles' recombination effects or promote carrier transportation<sup>21-23</sup>. Besides, the stability of core-shell materials increases due to the chemical and thermal inertness of the shell material<sup>24-26</sup>. In thin-film solar cells, shell thicknesses of less than 10 nm are usually adopted to realize large localized electromagnetic field and controllable carrier transportation properties<sup>13,22,23</sup>. However, the interaction mechanism between metal-dielectric core-shell nanostructures and the high-efficiency

MJSCs was still unexplored.

The difficulty partly originates from the large-scale fabrication method to organize nanometer-sized metal-dielectric composite nanostructures into centimeter-sized macro nanocoatings for solar cells. Top-down techniques face problems in the fabrication of three dimensions (3D) and multi-material nanostructures, limiting the enhancement research<sup>5</sup>. While bottom-up techniques, such as self-assembly methods, show advantages over shape control and multi-composite synthesis, benefiting from the chemically synthesized nanoparticles<sup>27-33</sup>. Nevertheless, the nanostructures using bottom-up approaches usually feature random particle distribution. The aggregation of nanoparticles and the resultant coupling effect are unavoidable, resulting in a deterioration of the efficiency of the devices<sup>34</sup>. In this account, interparticle coupling engineering in the self-assembly nanocoatings may be a solution to this problem.

Moreover, direct visualization strategies of the photoelectrical response of MJSCs at the submicrometer scale are still to be developed. Micro-region measurements have been demonstrated as useful strategies for direct optical or electrical characterization of plasmonic nanostructures at the nanoscale<sup>35-37</sup>. For example, the insight into plasmonic nanostructures' unique optical properties such as nonlocal effects<sup>38</sup>, strong-coupling regime<sup>39</sup>, electrically driven plasmonic sources<sup>40</sup>, and inhomogeneous plasmonic field<sup>41</sup> have been studied at the single-particle level using the micro-region spectroscopy. Micro-region scanning photocurrent microscopy (SPM), using a focused laser beam as the excitation, has been used to study the response of single-junction p-n junction devices<sup>34,42-44</sup> and plasmonic hot-electron photodetectors<sup>45,46</sup>. Nevertheless, when applied to MJSCs, limited by a series-connection condition, a single laser beam could not give a net photocurrent. Different illumination and testing strategies are needed.

Herein, we present the self-assembly of plasmonic Ag@SiO<sub>2</sub> core-shell nanocoating for efficiency enhancement on high-efficiency bulk InGaP/GaInAs/Ge MJSCs. We describe the device structure, investigate the plasmonic resonance properties (both near-field and far-field) and the response of the MJSCs with a single core-shell nanostructure with different shell thickness, demonstrate the self-assembly strategy of Ag@SiO<sub>2</sub> core-shell nanostructures, and make a comparison between experimental random-distributed coating enhancement and simulational periodic array enhancement. We also show that multi-wavelength enhancement results of the Ag@SiO<sub>2</sub> core-shell nanocoating can be directly observed under an infinity optical microscope with a double excitation strategy. Further,

we predict the relative enhancement could be reached with optimized structural parameters.

## Results

**Ag@SiO<sub>2</sub> core-shell nanostructures for plasmon-enhanced MJSCs.** The proposed device structure of InGaP/GaInAs/Ge MJSCs is shown schematically in Fig. 1a, where the Ag@SiO<sub>2</sub> core-shell nanostructure is put upon the window layer of the MJSCs devices. We first simplified the model to a single Ag@SiO<sub>2</sub> nanostructure with different shell thickness ( $t_{shell}$ ) atop InGaP-GaAs-Ge MJSCs (details are shown in Supplementary Fig. 1), where the solar cell area  $W^2$  was set to 10-folds of the projected area of the Ag@SiO<sub>2</sub> nanostructure. We calculated the all-optical simulation results using the 3D finite element method (FEM) under the assumption that internal quantum efficiency equal to 100%<sup>16</sup>, and modeling details will be introduced in the Methods section. Considering the current of InGaP-GaAs-Ge MJSCs is constrained by the top and middle subcells<sup>16</sup>, we only studied the optical responses of the upper two subcells.

As shown in Fig. 1b, if there is no shell (namely,  $t_{shell} = 0$ ), the current density in the top cell would not increase, which is similar to the previous results<sup>17</sup>. As  $t_{shell}$  increases from 2 nm to 90 nm, short-circuit current density of the top cell ( $J_{top\ cell}$ ) shows an increasing tendency first, followed by a dropping tendency with a maximum current density at a shell thickness of 50 nm. While the short-circuit current density of the middle cell ( $J_{middle\ cell}$ ) increases monotonically in this range. And  $J_{middle\ cell}$  is larger than  $J_{top\ cell}$  at all conditions, so we conclude that  $J_{top\ cell}$  determines the short-circuit current density ( $J_{sc}$ ) of the series-connected MJSC with Ag@SiO<sub>2</sub> nanostructures. To elucidate the enhancement mechanism, we compared the scattering intensity patterns for different shell thickness in Fig. 1c-d (3D scattering pattern at the wavelengths of 375 nm, 410 nm, and 450 nm referred to Supplementary Movies 1, 2, and 3, respectively). As illustrated, the scattering intensity of the Ag@SiO<sub>2</sub> could be modulated by the shell thickness. In our case, the maximum forward scattering (scattering into the MJSC) intensity (~1000 folds larger than the intensity of the bare Ag nanosphere) was achieved at  $t_{shell} = 50$  nm, while a thicker shell would lead to increased backward scattering intensity.

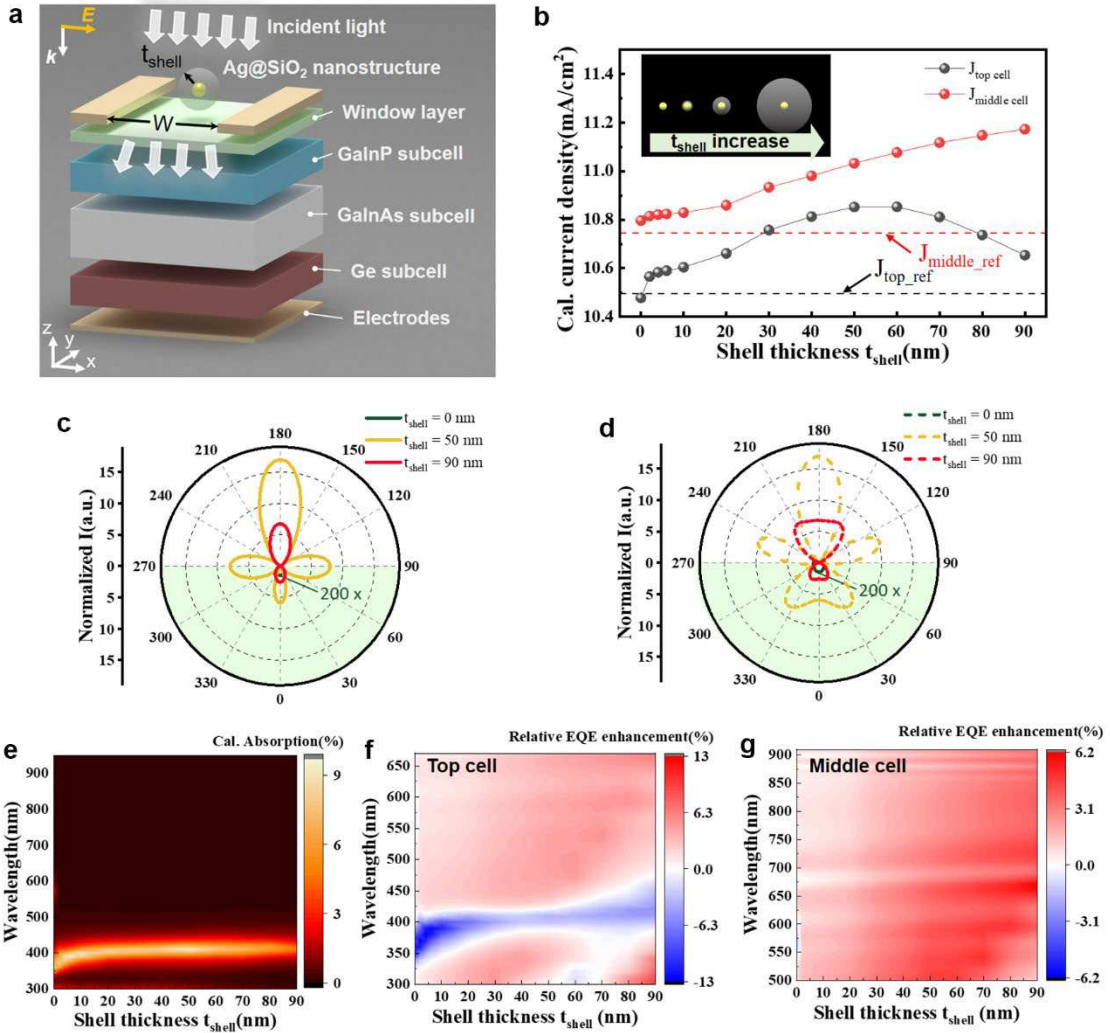


**Fig. 1** Plasmonic enhancement by Ag@SiO<sub>2</sub> nanostructures on MJSCs. **a** Schematic structure of Ag@SiO<sub>2</sub> atop a GaInP-GaInAs-Ge MJSC. **b** Calculated current density of top and middle solar cell with different  $t_{shell}$ . Calculated normalized scattering intensity patterns for the scattering planes parallel (**c**) and perpendicular (**d**) to the polarization of the incident wave ( $\lambda = 410$  nm). **e** Calculated Ag@SiO<sub>2</sub> absorption under different  $t_{shell}$ . Calculated relative EQE enhancement of top (**f**) and middle (**g**) cell under different  $t_{shell}$ .

Meanwhile, the absorption of Ag nanoparticle (Fig. 1e) and the relative external quantum efficiency (EQE) enhancement (Fig. 1f-g, Supplementary Fig. 2 for EQE original data) of subcells (top cell and middle cell) were calculated. The absorption peak of Ag@ SiO<sub>2</sub> nanostructures redshifts from 370 nm to 410 nm with the increasing  $t_{shell}$ , while absorption intensity slightly changes and reaches a maximum when  $t_{shell} = 50$  nm. Nevertheless, we notice that the EQE drop of the top cell near the Ag absorption region is the smallest when  $t_{shell} = 50$  nm, indicating more incident photons are preferentially scattering into the top cell near the plasmonic resonance wavelength region with the assistance of 50 nm SiO<sub>2</sub> shell. We also notice when  $t_{shell}$  further increase to 90 nm, although the absorption of Ag is gradually reduced, the EQE decreases near the plasmonic resonance region,

suggesting more photons are scattering backward into the air. Meanwhile, the EQE of the middle solar cell is enhanced almost at all wavelengths and all thicknesses. Therefore, a single Ag@SiO<sub>2</sub> nanostructure could improve the efficiency of the MJSC through scattering management regardless of the existence of the plasmonic absorption.

To study the influence of aggregates on the response of MJSCs, we simulated different aggregation types with the same surface coverage ( $\sim 48 \text{ NP}/\mu\text{m}^2$ ) of bare Ag nanospheres and Ag@SiO<sub>2</sub> core-shell nanostructures on the MJSCs. As shown in Fig. 2a, type I is monodisperse, represented by a periodic array with the same interparticle distance. Type II, III, and IV are dimer, tetramer, and trimer with single nanostructure atop as featured structures. The electrical field distributions of the Ag nanospheres and Ag@SiO<sub>2</sub> nanostructures are also depicted in Fig. 2a. Localized electric field enhancement up to 270 is observed at the Ag nanospheres gap, indicating the strong interparticle coupling without the shell. By stark contrast, the maximum electric intensity in Ag@SiO<sub>2</sub> aggregates is  $\sim 11$ , which means the plasmonic coupling is suppressed by  $\sim 22 \text{ nm}$  SiO<sub>2</sub> shell. The absorption spectra further show the plasmonic coupling of Ag and Ag@SiO<sub>2</sub> nanostructures, where absorption spectra of Ag aggregates show multiple absorption peaks while Ag@SiO<sub>2</sub> aggregates show similar absorption curves compared to the monodisperse condition (Fig. 2b and Fig. 2e). The EQE of the top and middle solar cell were calculated to study the spectral response of different structures (Fig. 2c and Fig. 2f). Interestingly, unlike Ag nanosphere aggregates, Ag@SiO<sub>2</sub> nanostructures studied here yields similar normalized EQE spectra of the top cell. To estimate the efficiency enhancement of InGaP-GaAs-Ge MJSCs under the solar spectrum of AM1.5G, we calculated the top and middle subcells' current density in Fig. 2d and Fig. 2g. Although the  $J_{middle \text{ cell}}$  increases slightly for Ag nanospheres aggregates, the  $J_{top \text{ cell}}$  decreases when aggregation happens. On the contrary, both  $J_{top \text{ cell}}$  and  $J_{middle \text{ cell}}$  of Ag@SiO<sub>2</sub> aggregates increase. Thus, the Ag@SiO<sub>2</sub> core-shell aggregates yield similar enhancement results as monodispersed core-shell nanostructures, which means the self-assembly Ag@SiO<sub>2</sub> core-shell nanocoating will result in a robust plasmonic enhancement.

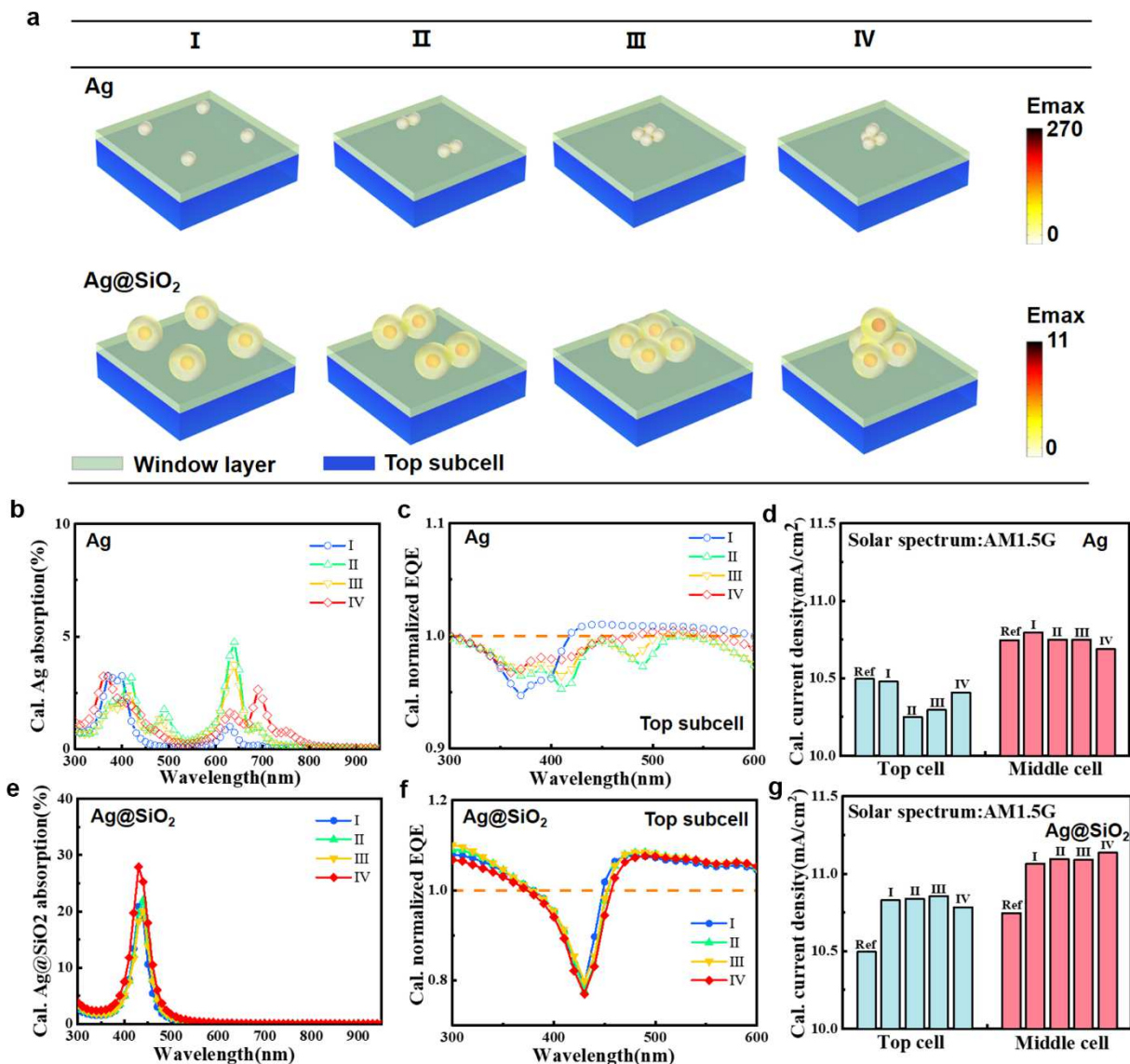


**Fig. 2** 3D FEM simulation of different types of aggregates atop of InGaP-GaAs-Ge MJSCs. **a** Illustrations of different type aggregates and the electrical field distribution in Ag (at 640 nm) and Ag@SiO<sub>2</sub> (at 410 nm) nanostructures. **b** Calculated Ag absorption. **c** Calculated normalized EQE of top subcell with Ag nanostructures. **d** Calculated  $J_{sc}$  of top subcell and middle subcell with Ag nanostructures. **e** Calculated Ag@SiO<sub>2</sub> absorption. **f** Calculated normalized EQE of top subcell with Ag@SiO<sub>2</sub> nanostructures. **g** Calculated current densities of top subcell and middle subcell with Ag@SiO<sub>2</sub> nanostructures.

**Nanocoating fabrication and characterization.** As proof of concept, we synthesized the Ag@SiO<sub>2</sub> experimentally, and the characteristic transmission electron microscopy (TEM) graphs in Supplementary Fig. 3 shows both Ag cores and Ag@SiO<sub>2</sub> core-shell nanostructures are large-scale monodispersed and well-dispersed. The typical diameter of Ag cores is ranged from 22 nm to 34 nm, with a mean diameter of 29 nm. Besides, the thickness of the SiO<sub>2</sub> shell is in the range of 16 to 30 nm,

with a mean thickness of 22 nm. Ag@SiO<sub>2</sub> core-shell nanostructures' surfaces are negative-charged and abundant with -OH, which facilitate the bonding with poly-L-lysine through electrostatic forces or a dehydration reaction<sup>47</sup>. The self-assembly process involves the following steps (Fig. 3a). First, the InGaP/GaInAs/Ge MJSC were inverted floated (supported by the water's surface tension) upon the poly-L-lysine solution for 5 minutes, enabling the absorption of the front side only. Then, excess poly-L-lysine molecules were washed by ultra-pure water to ensure that no optical-thick layer exists. After that, the MJSC was immersed in the ethanol solution of Ag@SiO<sub>2</sub> core-shell nanostructures for different times (1,5 and 15 minutes), followed by washing with ultra-pure water to remove the unbound nanostructures. We performed an element analysis of MJSCs after the self-assembly process. Energy-dispersive X-ray spectrometer (EDS) results of the bare MJSC and the MJSC after 15 min nanostructure assembly are provided in Supplementary Fig. 3. We found Ag and Si elements in the MJSC after the self-assembly process, further verifying the successful self-assembly of Ag@SiO<sub>2</sub> core-shell nanostructures. We have already proved that poly-L-lysine treatment has a negligible effect on the solar cells' electrical parameters in Reference 47. To verify the existence of poly-L-lysine, we examined element N, which is a characteristic element in poly-L-lysine. A trace amount of N element is found in the sample after the self-assembly process, while no N element was detected in the bare MJSC.

To determine the surface coverage of Ag@SiO<sub>2</sub> nanostructures atop InGaP/GaInAs/Ge MJSCs, we analyzed the scanning electron microscopy (SEM) characterizations shown in Fig. 3b-d. As time increases from 1 min to 15 min, the distribution density of Ag@SiO<sub>2</sub> core-shell nanostructures continually increase. However, when the assembly time further increases to 30 min, there is no perceptible increase in distribution density (Supplementary Fig. 4). SEM graphs near the grid regions and the large-area views provided in Supplementary Fig. 5 show the large-area consistency at the whole surface of MJSCs. Further statistical analysis of SEM graphs supplies the surface coverage data of Ag@SiO<sub>2</sub> core-shell nanocoatings on MJSCs. The assembly time of 1 min, 5 min, and 15 min yields ~4, ~18, and ~47 nanoparticles per square micrometer (NP/μm<sup>2</sup>), respectively (Fig. 3e). Additionally, single-layer dimers and multimers exist in all of the samples. Compared with monodispersed TEM graphs, it indicates the introduction of those aggregates may result in the self-assembly process. We determined the structural types in the self-assembly layer (Fig. 3f). Only 50%-70% of structures are single, while the multimer ratio increased along with the increased surface coverage of nanostructures.

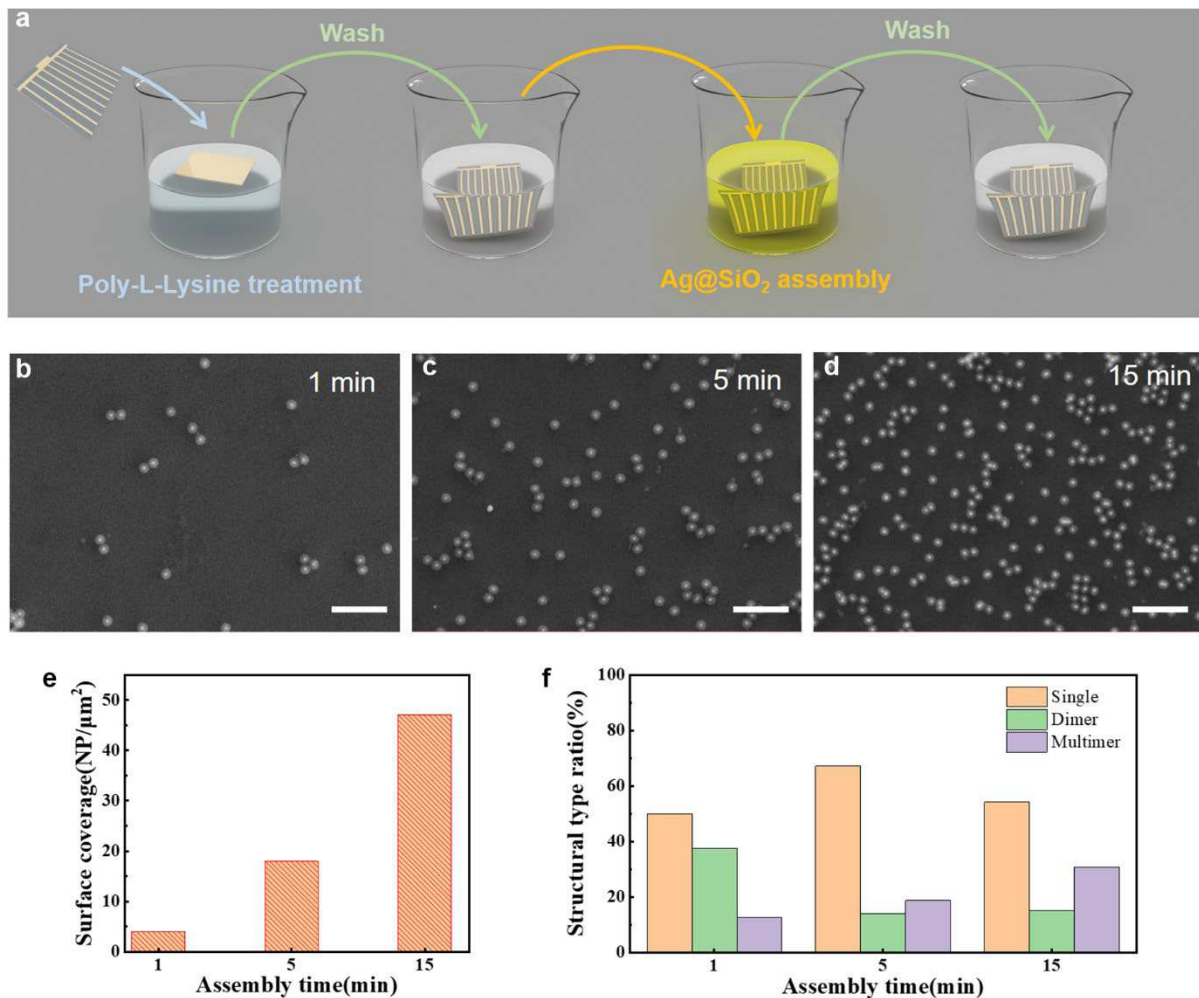


**Fig. 3 SEM analysis of Ag@SiO<sub>2</sub> core-shell nanocoatings.** SEM image of different self-assembly time 1 min(b), 5 min(c), and 15 min(d). e Surface coverage analysis of the self-assembly nanocoating under different times. f Structural type analysis of the Ag@SiO<sub>2</sub> nanostructures in the self-assembly nanocoating.

**Macro photoelectrical response measurement.** Aimed to confirm the robust enhancement results experimentally, we compared the enhancement between the experimental random distributed nanostructures and the simulational periodic nanostructure arrays (Fig. 4). To fully recover the real condition, we first let the surface coverage similar to our self-assembly samples. The simulational period is set to be 500 nm (W1), 230 nm (W2), 145 nm (W3), corresponding to a surface coverage of 4, ~18, and ~48 NP/μm<sup>2</sup>, respectively. As shown in Fig. 4b and Fig. 4e, when the wavelength exceeds 450 nm, the EQE of the top subcell increases with the assembly time. However, at the wavelength region near plasmonic resonance of Ag@SiO<sub>2</sub> nanostructures, the top subcell EQE reduces along with the increased assembly time. That is to say, near the plasmonic resonance wavelength, even though the strong antireflection happens (Supplementary Fig. 6), strong absorption of the Ag@SiO<sub>2</sub> nanocoating deteriorates the EQE. So, there is a tradeoff between the photoelectrical responses at different

wavelengths, similar to the previously reported results using Au or Ag nanoparticles<sup>17</sup>. Besides, the EQE of the middle subcell slightly increased with the adding of nanostructured layers at the entire wavelength range. We also normalized the EQE of the MJSCs with a nanostructured layer to the Ref device (Fig. 4c and Fig. 4f). Although the EQE curve shows some difference between experimental and simulational results due to optical constants difference from doping, the normalized EQE curves show an excellent consistency between experiment and simulation. As a result, the  $J_{sc}$  data derived from EQE data also show a similar increasing trend (Fig. 4d and Fig. 4g). With the self-assembly time increases, the experimental  $J_{sc}$  increases from 9.76 mA/cm<sup>2</sup> to 9.79 mA/cm<sup>2</sup> (1 min), 9.93 mA/cm<sup>2</sup> (5 min) and 10.17 mA/cm<sup>2</sup> (15 min), with relative enhancement of 0.31% (1 min), 1.74% (5 min) and 4.20% (15 min). The simulational  $J_{sc}$  varies from 10.49 to 10.55 mA/cm<sup>2</sup> (W1), 10.65 mA/cm<sup>2</sup> (W2), 10.79 mA/cm<sup>2</sup> (W3), and the relative enhancement are 0.57% (W1), 1.53% (W2), and 2.86% (W3). Thus, we conclude that the aggregates in self-assembly methods did not alleviate the enhancement. We also verify that the simulational periodic arranged Ag@SiO<sub>2</sub> nanostructures could be used to predict the enhancement of experimental random distributed Ag@SiO<sub>2</sub> nanostructures, with a shell thickness of more than 20 nm.

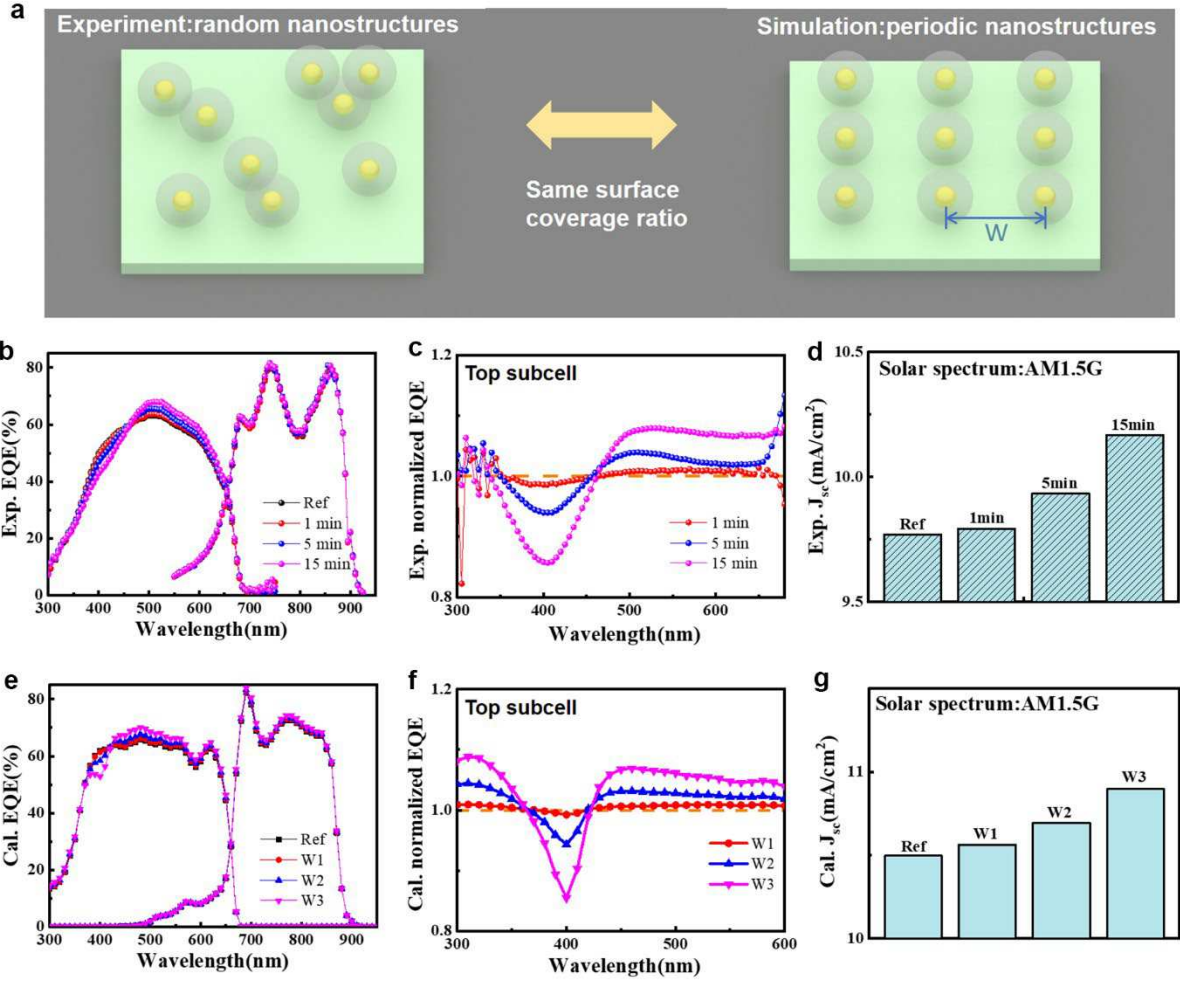


**Fig. 4 Macro enhancement comparison between experimental random distributed and simulational periodic nanostructures.** **a** Schematic of experimental and simulational structure on MJSCs. Experimental EQE (**b**), normalized EQE of the top cell (**c**), and  $J_{sc}$  derived from EQE data (**d**). Simulational EQE (**e**), normalized EQE of the top cell (**f**), and  $J_{sc}$  derived from calculated EQE data (**g**).

We listed the electrical parameters under AM1.5G in Table 1. Following the increased assembly time from 1 min to 15 min, the  $J_{sc}$  boosts from 10.34 mA/cm<sup>2</sup> to 10.83 mA/cm<sup>2</sup> (15 min), yielding a power conversion efficiency (PCE) increased from 22.80% to 23.45%. Additionally, similar surface coverage samples of assembly time of 15 min and 30 min yields similar efficiency (Supplementary Table 1). So, we concluded that there might be a positive correlation between the surface coverage of Ag@SiO<sub>2</sub> core-shell nanocoatings and  $J_{sc}$ . The maximum PCE enhancement (2.85%) is lower than that of  $J_{sc}$  (4.7%), indicating that the nanostructured layer leads to both optical effects and electrical influences. Just as mentioned before, the  $V_{oc}$  appears no noticeable change with the increased surface coverage. By contrast, we found that the fill factor of the MJSCs is slightly decreased from 85.53% to 84.35%, in accord with the increased surface coverage of Ag@SiO<sub>2</sub> nanocoatings. As SiO<sub>2</sub> shells insulate the

Ag nanospheres and the MJSC, recombination effects of the nanostructures almost eliminate. It suggests the main reason of the deterioration in the fill factor may lie in the inevitable assembly of Ag@SiO<sub>2</sub> core-shell nanostructures on the electrodes.

**Table 1 Electrical parameters of MJSCs with different self-assembly time**

Description	V <sub>oc</sub> (V)	J <sub>sc</sub> (mA/cm <sup>2</sup> )	Fill factor(%)	Efficiency(%)
Ref	2.58±0.01	10.34±0.17	85.53±0.28	22.80±0.36
1 min	2.56±0.01	10.51±0.06	84.94±0.06	22.93±0.12
5 min	2.56±0.01	10.71±0.08	84.65±0.08	23.25±0.14
15 min	2.56±0.01	10.83±0.10	84.35±0.16	23.45±0.19

**Micro-region photoelectrical response measurement.** To unveil the enhancement effects of Ag@SiO<sub>2</sub> core-shell nanocoatings directly on the micro-scale, we designed and built a micro-region photoelectrical response measurement system (Supplementary Fig. 7). The submicrometer-scale SPM measurement is based on an infinity optical microscope with a double excitation strategy described in Fig. 4a. Due to the current-constrained condition in series packed MJSCs, all other subcells are supposed to supply larger currents when one subcell is tested. The wide-spectral light from a tungsten halogen lamp processed by a Kohler illuminating path and a designed color filter act as the biased light for MJSCs. As an example, for the photocurrent measurement of the InGaP subcell in a triple-junction InGaP/GaInAs/Ge solar cell, the wide-spectral light is filtered by an 800 nm long-pass filter for the excitation of the GaInAs and Ge solar cell. Frequency-modulated wavelength-tunable laser functions as the signal light, which power could be delicately nudged to ensure the current-limited condition. A home-made MJSC microscopic holder and 4-wire connection are used to test the electrical signal. The modulated photocurrent is collected and processed by a current preamplifier, a lock-in amplifier, and a digital source-measure unit (SMU). Moreover, a biased voltage is provided from the SMU. The focused laser and biased light can be scanned using a piezoelectric travel translation stage with X/Y motors when SPM measurements are performed. Controlled by a home-designed Labview program, the modules mentioned above enable efficient in-situ micro-region optical and SPM measurements of MJSCs.

The device with a self-assembly time of 5 min was investigated for relative uniform distribution with fewer multilayer aggregates. We set a micro-region with an area of 8 × 8 μm as the region of interest. Before testing, we partly wiped out the Ag@SiO<sub>2</sub> core-shell nanocoating using non-dusting

whipping paper, aiming to get a micro-region partly covered by the nanocoating and partly bare. In this way, we enable direct observation of the enhancement induced by the core-shell nanocoating. Fig. 4b-c show the brightfield and darkfield optical images of the device's surface, and the corresponding optical path is shown in Supplementary Fig. 8. The white frame lines define the boundary of the nanocoating and bare surface. We can discern the region with/without nanocoating from the brightfield image, but the negligible scattering from the monolayer nanostructured layer makes little difference in the darkfield image.

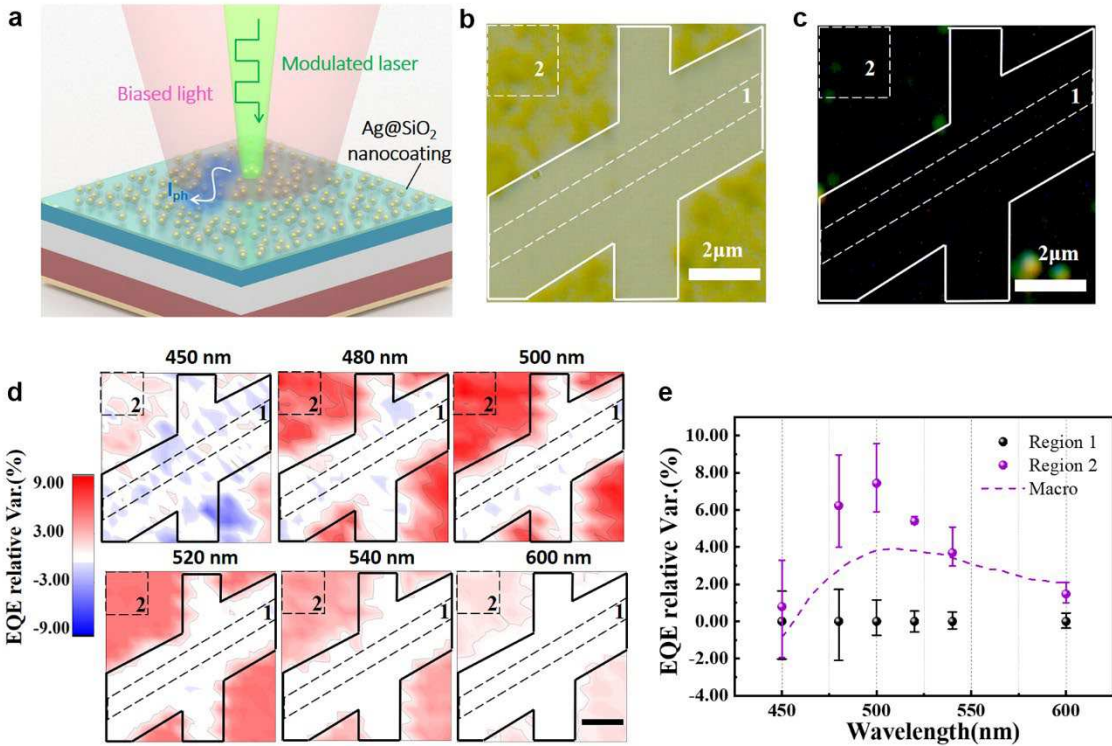


**Fig. 5 Micro-region SPM study for InGaP-GaAs-Ge MJSCs with the Ag@SiO<sub>2</sub> core-shell nanocoating (assembly time, 5 min).** **a** Schematic graph of the submicrometer-scale photoelectrical response measurement for MJSCs. The brightfield (**c**) and darkfield images (**d**) of the MJSCs with partly-removed Ag@SiO<sub>2</sub> core-shell nanocoating (assembly time, 5 min). The Ag@SiO<sub>2</sub> nanostructures in the region surrounded by the white frame lines were wiped out. **d** The wavelength-dependent EQE relative variation images of the same region as the optical images shown in **a-b**. **e** EQE relative variation analysis of the background (region 1) and the Ag@SiO<sub>2</sub> core-shell nanocoating (region 2) under the excitation of different wavelengths. The dashed line presents the top subcell's macro normalized EQE curve with an assembly time of 5 min. The error bars show the absolute variations in the specific region.

Using the proposed SPM for the MJSC, we attained the photocurrent ( $I_{ph}$ ) mapping images (17 × 17 pixels) for the MJSC under the laser excitation with different wavelengths. For comparison between micro and macro measurements, we define micro EQE relative variation as  $\Delta EQE/EQE_{back}$ , where  $\Delta EQE$  is the difference between EQE of the location to be measured and the EQE of background

( $EQE_{back}$ , without nanostructured layer). Similarly, the photocurrent relative variation is  $(I_{ph} - I_{back})/I_{back}$  ( $\Delta I_{ph}/I_{back}$ ). And we transform the photocurrent maps into EQE relative variation maps with the following relation,

$$I_{ph} = qP_{laser} \cdot \frac{\lambda}{hc} \cdot EQE \quad (1)$$

$$\Delta EQE/EQE_{back} = \Delta I_{ph}/I_{back} \quad (2)$$

where  $I_{ph}$  is the generated photocurrent,  $P_{laser}$  is the power of the laser just after the microscope objective. To diminish the random error, we set mean  $I_{ph}$  of region 1 (27 pixels) as  $I_{back}$ . Region 1 is defined as the equation  $0.5x + 1 \leq y \leq 0.5x + 2$  ( $0 \leq x, y \leq 8$ ), where the origin was set as the lower-left corner. As we have discussed, the  $J_{sc}$  of the top subcell mainly contributes to the current enhancement of the whole device, so only the EQE relative variation of the top subcell is obtained (Fig. 5c). The EQE enhancement of the top subcell under different excitation wavelengths varies differently. In the mapping images, the red color, blue color, and white color represent an increase, a decrease, and no distinct change relative to  $EQE_{back}$ , respectively. The contrast between the double-sides of the black line border in the EQE images directly displays the enhancement effect of the Ag@SiO<sub>2</sub> core-shell nanocoating. No noticeable enhancement or suppression was found at 450 nm, but definite enhancements were achieved at the wavelengths longer than 480 nm with a maximum value of ~10%. Statistical analysis was conducted to show the average enhancement and variation level of the proposed method in Fig. 5d-f and Supplementary Table 2-3, where the area of region 2 was  $2 \times 2 \mu\text{m}$  (25 pixels). In region 1, the absolute variation is ~2% at the wavelengths of 450 nm and 480 nm, near 1% (or smaller than 1%) at other wavelengths. Small changes in the background area may be related to the nonuniformity of the surface, the fluctuation of laser power, the background noise in the current extraction circuit, and the spectral response of the MJSC. The wavelength-dependent average enhancement of region 2 follows the same trend with the macro EQE test, with the maximum relative enhancement at 500 nm. Additionally, the absolute variation of region 2 is similar to that of region 1, indicating the relatively uniform distribution of the Ag@SiO<sub>2</sub> core-shell nanocoating.

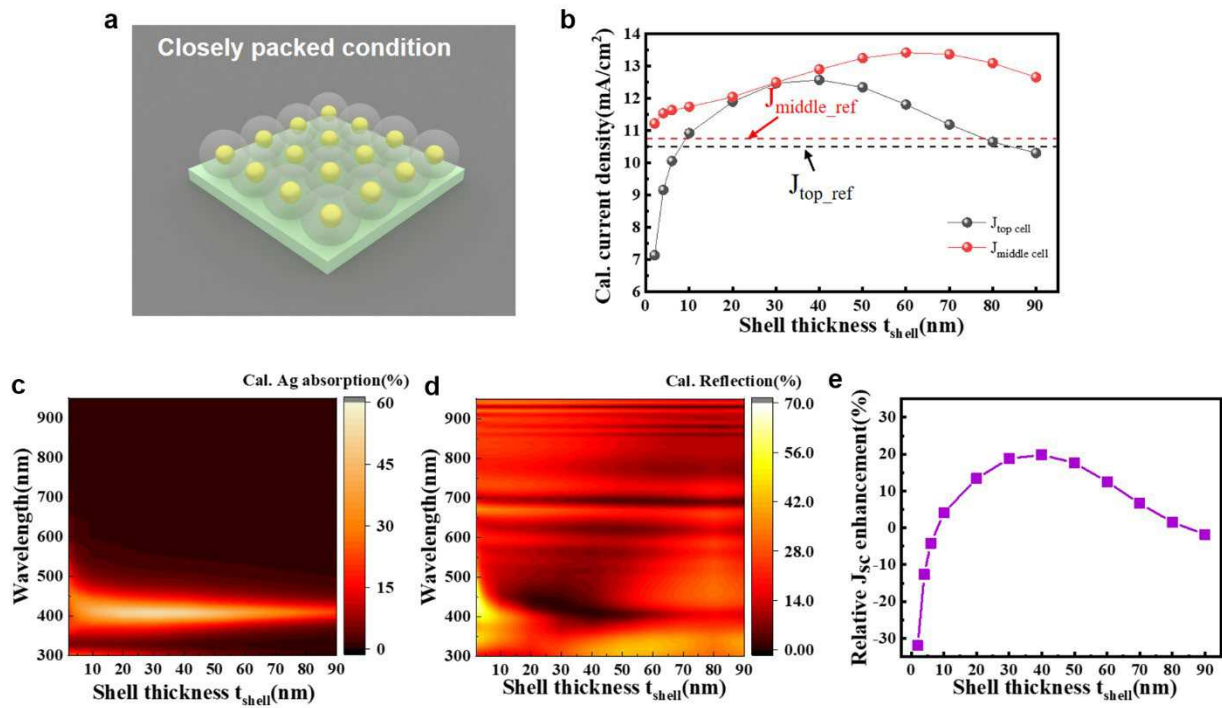


**Fig. 6 Simulation of closely packed Ag@SiO<sub>2</sub> nanostructure array atop the MJSC. a** Schematic of the MJSC with closely packed Ag@SiO<sub>2</sub> nanostructures. **b** Calculated Shell thickness-dependent current density of top and middle solar cell; the dashed line shows the current density without nanostructure. **c-d** Calculated Ag absorption and reflection of the MJSC with different shell thicknesses. **e** Relative  $J_{sc}$  enhancement of the MJSC with closely packed Ag@SiO<sub>2</sub> nanostructure array.

To explore the optimized parameters for MJSCs using Ag@SiO<sub>2</sub> nanostructures, we simulated the closely packed arrays of Ag@SiO<sub>2</sub> nanostructures (Fig. 6 and Supplementary Fig. 9). The schematic of closely packed nanostructures are shown in Fig. 6a, and we calculated the current density of the top cell and middle cell in Fig. 6b. The results are different from the well-dispersed single particle condition in Fig. 1b. Both  $J_{top\ cell}$  and  $J_{middle\ cell}$  show inflection points (at 40 nm for  $J_{top\ cell}$  and 60 nm for  $J_{middle\ cell}$ ). Besides, the absorption bandwidth of Ag nanocore gradually shrink with the increased  $t_{shell}$ , while the absorption intensity achieves the maximum value at a thickness of 40 nm (Fig. 6c). Fig. 6d shows the reflectance spectra of Ag@SiO<sub>2</sub> MJSCs with nanostructures, the lowest reflectance located in the Ag absorption peak in the thickness range of 30 to 90 nm, and the smallest reflectance is approaching 0%. At last, we calculated the shell thickness-dependent relative enhancement in Fig. 6e, and we found a  $J_{sc}$  enhancement of 19.92% (from 10.49 mA/cm<sup>2</sup> to 12.58 mA/cm<sup>2</sup>) when  $t_{shell} = 40$  nm, which may be experimentally achieved by multiple assembly processes or the Meyer rod method<sup>48</sup>.

## Discussion

We have demonstrated that Ag@SiO<sub>2</sub> self-assembly nanocoatings enable efficiency-boosting of InGaP-GaAs-Ge MJSCs at macro and micro scale. We show a relatively thicker shell (about 20-50 nm) is needed for bulk MJSC enhancement compared to the thin-film solar cell or plasmon-enhanced spectroscopy applications. The enhancement mechanism mainly contributes to enhanced far-field forward scattering while the near-field coupling needs to be suppressed. Based on our results, we estimated a  $J_{sc}$  enhancement of 19.92% for the close-packaged Ag@SiO<sub>2</sub> condition, comparable to the enhancement of antireflection film techniques. Moreover, the relatively simple fabrication method and thinner thickness make them more competitive for photovoltaic applications. We point out that the dielectric shell could be replaced with semiconductor materials such as TiO<sub>2</sub>, ZnO<sup>49,50</sup>. We also predict that metal-dielectric super-scattering nanostructures with designed electric and magnetic dipolar resonances<sup>42,43</sup> may further boost efficiency. Additionally, we emphasize the importance of the multi-scale characterization for plasmon-enhanced MJSCs. With this strategy, not only can we compare the macro performance of the MJSCs, but also directly observe and study the plasmonic enhancement with a submicrometer resolution. We believe our findings will open a new path for developing ultrahigh efficiency MJSCs using nanophotonics.

## Methods

**Materials.** Silver nitrate (AgNO<sub>3</sub>, 99.9%), ascorbic acid (AA, >99.5%), Tetraethyl orthosilicate (TEOS, 98%), and sodium hydroxide solution (NaOH, ≥98%) were purchased from Sigma-Aldrich. Absolute ethanol ( $\geq 95\%$ ) and cetyltrimethylammonium bromide (CTAB, >99.0%) was purchased from sinopharm chemical reagent Co. Ltd. Poly-L-lysine was bought from Xiya Regent. Milli-Q Ultrapure water (resistivity  $> 18.2 \text{ M}\Omega \text{ cm}$ ) was utilized in all experiments. All chemicals in the experiment are used with no further purification. The Shanghai Institute of Space Power-Source provided triple-junction InGaP-GaAs-Ge solar cells. The solar cells (area:  $3.14 \text{ cm}^2$ ) were cut from a single epitaxial wafer for similar original spectral response and efficiency.

**Synthesis of Ag@SiO<sub>2</sub> core-shell nanostructure.** The Ag@SiO<sub>2</sub> core-shell nanostructure was synthesized using a one-pot method modified from the previous work<sup>51</sup>. Briefly, 3 mL freshly prepared AgNO<sub>3</sub> (0.1 M) was added to 60 mL CTAB (2.5 mM) under moderate stirring for 2 minutes, followed by adding 4.2 mL AA (0.1 M) solution and stirring for another 5 minutes, 1.68 mL NaOH (0.5 M) was

further added and stirred for 15 minutes. After those steps, Ag nanoparticle was synthesized, an aliquot of 1 mL was extracted and centrifuged one time before characterization. Immediately after the synthesis of Ag nanospheres, 150  $\mu$ L TEOS and 15 mL ethanol were added to the Ag nanosphere solution, another 975  $\mu$ L NaOH (0.5 M) was injected to adjust the PH of the solution to  $\sim$ 10.9 for proper coating speed. The SiO<sub>2</sub> coating process lasts about 3 hours. The resultant products were centrifuged several times using ethanol and condensed to 5 mL for further use and characterization.

**Ag@SiO<sub>2</sub> core-shell nanostructures characterization.** The Ag@SiO<sub>2</sub> core-shell nanostructures' structural parameters were characterized by TEM (Fei Tecnai G20) with an acceleration voltage of 200 kV, and ImageJ software was used to analyze the statistical results. The extinction spectra were acquired from a fiber spectrometer (Nova, Ideaoptics Co Ltd). The Ag@SiO<sub>2</sub> core-shell self-assembly nanocoating was characterized by a scanning electron microscope (SEM, Zeiss Ultra Plus) operating at 5 kV-10 kV. Elemental compositions of the self-assembly layer were also studied by an energy-dispersive X-ray spectrometer (EDS).

**Macro measurements of MJSCs.** The electrical properties of solar cells are measured with a high-precision SMU (Keithley 2651), and the illumination was simulated with a 1000 W xenon lamp equipped with an AM1.5 filter (CrownTech Inc.). A standard reference cell (VLSI Standards Inc., SRC-1000-TC-K-QZ-C) is used to calibrate. The reflection spectra of MJSCs were also taken from a fiber spectrometer (Nova, Ideaoptics Co Ltd) coupled with an integrating sphere. The solar spectral power density of AM1.5G is obtained from ASTM G173-03 reference spectra derived from SMARTS. The external quantum efficiency of the MJSC was recorded with a solar cell quantum efficiency system (PV Measurements, QEX10). Intending to discern the current contribution from each subcell, we calculated  $J_{sc}$  of the top subcell and the middle subcell with the integral equation (3),

$$J_{sc} = q \int_{\lambda_1}^{\lambda_2} P_{AM1.5G}(\lambda) \cdot \frac{\lambda}{hc} \cdot EQE(\lambda) d\lambda \quad (3)$$

where  $P_{AM1.5G}$  is the solar spectral power density of AM1.5G,  $q$  is the elementary charge,  $h$  is the Planck constant,  $c$  is the speed of light in free space,  $\lambda$  is the wavelength.

**Micro-region imaging measurement.** Brightfield and darkfield optical images are collected at the same location using a Nikon inverted microscope (Ti-U) with a 100 W tungsten halogen lamp. A 100 $\times$  0.80 NA objective lens (Nikon Plan Fluor ELWD 100X) was used to collect both the bright and dark field images and spectra. The optical images are collected by a scientific color CCD (Qimaging

MicroPublisher 3.3).

**SPM measurement for MJSCs.** SPM includes the custom-designed electrical measurement fixture, which can be perfectly matched with Nikon dark-field microscope and the piezoelectric travel translation stage (TANGO Desktop, Märzhäuser). Monochromatic radiation was created through the super-continuum white-light source (YSL Photonics, SC-PRO) and acousto-optic tunable filter (YSL AOTF-PRO) through an optical cage laser beam expander system and an aperture to reduce the divergence angle of light and filtered by the color temperature filter (LB-165, Thorlabs). The mapping length is 8  $\mu\text{m}$  with a step of 500 nm. A chopper working at a frequency of 500Hz was used to get the photocurrent, and a current preamplifier (Stanford SR570) and lock-in amplifier (Hengbing Instrument) was used to suppress the dark current. A high-precision SMU (Keithley 2450) was used to record the data and supply the biased voltage. The laser beam's power was recorded by a Newport 843-4-USB power meter with a 918D-SL-OD1R Si photodetector. The focused laser's power is 450 nW, 560 nW, 505 nW, 665 nW, 965 nW, and 740 nW at the wavelength of 450 nm, 480 nm, 500 nm, 520 nm, 540 nm, and 600 nm, respectively. The focused laser and biased light's spot size is estimated as  $\sim 1.5 \mu\text{m}$  and 300  $\mu\text{m}$ .

**3D FEM simulation.** We used the periodic boundary conditions for the x- and y-axis for easier surface coverage control in the simulation. Perfect matched layer (PML) conditions were applied along the z-axis, which diminishes the unexpected reflection. Two ports between the PML layers and the device's geometry were set for excitation (planar wave polarized in the x-direction). The permittivity of silver was fitted using the Lorentz-Drude model<sup>52</sup>. The optical constants of SiO<sub>2</sub>, GaInAs, Ge are linearly interpolated from the handbook<sup>53</sup>. The optical constants for AlInP, GaInP, AlGaInP, and AlGaAs are adopted from Ref<sup>54-57</sup>.

For the absorption of Ag@SiO<sub>2</sub>, the top cell and the middle cell can be expressed as

$$A = \int_V \frac{\omega}{2} \text{Im}(\varepsilon(\omega)) \varepsilon_0 |\mathbf{E}(\mathbf{r})|^2 d^3r \quad (4)$$

where  $\mathbf{E}$  is the electric field intensity,  $\varepsilon$  is the dielectric of the material,  $\varepsilon_0$  is the permittivity of vacuum, and the  $\omega$  is the angular frequency of light. The current density was also calculated from equation (3) with the absorption of each subcell.

For far-field scattering pattern simulation, we used a scattering field formulation, triggered by the background field calculated by replacing the dielectric constants of the Ag@SiO<sub>2</sub> nanostructure

domain with the dielectric constants of the air. We further normalized the angle-distributed scattering power by geometric cross-section area of the Ag@SiO<sub>2</sub> for comparison of different shell thicknesses.

## Data availability

The data that support the findings of this study are available from the corresponding author upon reasonable request.

## Reference

- 1 Polman, A. & Atwater, H. A. Photonic design principles for ultrahigh-efficiency photovoltaics. *Nat. Mater.* **11**, 174-177 (2012).
- 2 Atwater, H. A. & Polman, A. J. N. M. Plasmonics for improved photovoltaic devices. *Nat. Mater.* **9**, 205-213 (2010).
- 3 Boriskina, S. V., Ghasemi, H. & Chen, G. J. M. T. Plasmonic materials for energy: From physics to applications. *Mater. Today* **16**, 375-386 (2013).
- 4 Erwin, W. R., Zarick, H. F., Talbert, E. M., Bardhan, R. J. E. & Science, E. Light trapping in mesoporous solar cells with plasmonic nanostructures. *Energy Environ. Sci.* **9**, 1577-1601 (2016).
- 5 Karg, M. *et al.* Colloidal self-assembly concepts for light management in photovoltaics. *Mater. Today* **18**, 185-205 (2015).
- 6 Fu, N. *et al.* Panchromatic thin perovskite solar cells with broadband plasmonic absorption enhancement and efficient light scattering management by Au@Ag core-shell nanocuboids. *Nano Energy* **41**, 654-664 (2017).
- 7 Kholmicheva, N. *et al.* Plasmonic nanocrystal solar cells utilizing strongly confined radiation. *ACS Nano* **8**, 12549-12559 (2014).
- 8 Liu, D. *et al.* Flexible near-infrared photovoltaic devices based on plasmonic hot-electron Injection into silicon nanowire arrays. *Angew. Chem. Int. Ed. Engl.* **55**, 4577-4581 (2016).
- 9 Mubeen, S. *et al.* On the plasmonic photovoltaic. *ACS Nano* **8**, 6066-6073 (2014).
- 10 Wang, Y. *et al.* In situ assembly of well-defined Au nanoparticles in TiO<sub>2</sub> films for plasmon-enhanced quantum dot sensitized solar cells. *Nano Energy* **44**, 135-143 (2018).
- 11 Yao, K. *et al.* Plasmonic metal nanoparticles with core-bishell structure for high-performance organic and perovskite solar cells. *ACS Nano* **13**, 5397-5409 (2019).
- 12 Wang, S. J., Su, D. & Zhang, T. Research progress of surface plasmons mediated photothermal effects. *Acta Phys. Sin.* **68** (2019).
- 13 Hanske, C., Sanzortiz, M. N. & Lizmarzan, L. M. J. A. M. Silica-coated plasmonic metal nanoparticles in action. *Adv. Mater.* **30**, 1707003 (2018).
- 14 Liu, S. *et al.* Au/Ag core-shell nanocuboids for high-efficiency organic solar cells with broadband plasmonic enhancement. *Energy Environ. Sci.* **9**, 898-905 (2016).
- 15 Geisz, J. F. *et al.* Six-junction III-V solar cells with 47.1% conversion efficiency under 143 Suns concentration. *Nat. Energy* **5**, 326 (2020).
- 16 Yang, L., Pillai, S. & Green, M. A. J. S. R. Can plasmonic Al nanoparticles improve absorption in triple junction solar cells. *Sci. Rep.* **5**, 11852-11852 (2015).
- 17 Hylton, N. P. *et al.* Loss mitigation in plasmonic solar cells: Aluminium nanoparticles for broadband photocurrent enhancements in GaAs photodiodes. *Sci. Rep.* **3**, 2874-2874 (2013).
- 18 Mellor, A., Hylton, N. P., Hauser, H., Thomas, T. & Ekins-Daukes, N. J. J. I. J. o. P. Nanoparticle scattering for

- multijunction solar cells: The tradeoff between absorption enhancement and transmission loss. *IEEE J. Photovolt.* **6**, 1678-1687 (2016).
- 19 Wang, Y. *et al.* Plasmon-directed polymerization: Regulating polymer growth with light. *Nano Res.* **11**, 6384-6390 (2018).
- 20 Shi, R. *et al.* Self-assembled Au/CdSe nanocrystal clusters for plasmon-mediated photocatalytic hydrogen evolution. *Adv. Mater.* **29**, 1700803 (2017).
- 21 Pazsoldan, D. *et al.* Jointly tuned plasmonic-excitonic photovoltaics using nanoshells. *Nano Lett.* **13**, 1502-1508 (2013).
- 22 Ye, T. *et al.* Performance enhancement of tri-cation and dual-anion mixed perovskite solar cells by Au@SiO<sub>2</sub> nanoparticles. *Adv. Funct. Mater.* **27**, 1606545 (2017).
- 23 Zhang, R. *et al.* Influence of SiO<sub>2</sub> shell thickness on power conversion efficiency in plasmonic polymer solar cells with Au nanorod@SiO<sub>2</sub> core-shell structures. *Sci. Rep.* **6**, 25036 (2016).
- 24 Ding, S.-Y. *et al.* Nanostructure-based plasmon-enhanced Raman spectroscopy for surface analysis of materials. *Nat. Rev. Mater.* **1**, 16021 (2016).
- 25 Li, C. Y. *et al.* "Smart" Ag nanostructures for plasmon-enhanced spectroscopies. *J. Am. Chem. Soc.*, 13784-13787 (2015).
- 26 Yin, H. *et al.* Plasmon enhanced quantum dots fluorescence and energy conversion in water splitting using shell-isolated nanoparticles. *Nano Energy* **42**, 232-240 (2017).
- 27 Fan, J. A. *et al.* Self-assembled plasmonic nanoparticle clusters. *Science* **328**, 1135-1138 (2010).
- 28 Zhang, X. Y. *et al.* Self-assembly of large-scale and ultrathin silver nanoplate films with tunable plasmon resonance properties. *ACS Nano* **5**, 9082-9092 (2011).
- 29 Begley, M. R., Gianola, D. S. & Ray, T. R. Bridging functional nanocomposites to robust macroscale devices. *Science* **364**, 1250 (2019).
- 30 Richardson, J. J., Bjornmalm, M. & Caruso, F. Technology-driven layer-by-layer assembly of nanofilms. *Science* **348**, aaa2491 (2015).
- 31 Montelongo, Y., Yetisen, A. K., Butt, H. & Yun, S. H. Reconfigurable optical assembly of nanostructures. *Nat. Commun.* **7**, 12002 (2016).
- 32 Li, S. *et al.* High-resolution patterning of solution-processable materials via externally engineered pinning of capillary bridges. *Nat. Commun.* **9**, 393 (2018).
- 33 Li, S. *et al.* Two-dimensional arrays self-assembled via interference of concentration modulation waves in drying solutions. *Mater. Horiz.* **6**, 507-514 (2019).
- 34 Sundararaian, S. P., Grady, N. K., Mirin, N. & Halas, N. J. Nanoparticle-induced enhancement and suppression of photocurrent in a silicon photodiode. *Nano Lett.* **8**, 624-630 (2008).
- 35 Huang, I. C. *et al.* 10 nm gap bowtie plasmonic apertures fabricated by modified lift-off process. *Appl. Phys. Lett.* **109**, 133105 (2016).
- 36 Quan, Q. *et al.* Single particle detection in CMOS compatible photonic crystal nanobeam cavities. *Opt. Express* **21**, 32225-32233 (2013).
- 37 Zhou, J., Chizhik, A. I., Chu, S. & Jin, D. Single-particle spectroscopy for functional nanomaterials. *Nature* **579**, 41-50 (2020).
- 38 Ciraci, C. *et al.* Probing the ultimate limits of plasmonic enhancement. *Science* **337**, 1072-1074 (2012).
- 39 Chikkaraddy, R. *et al.* Single-molecule strong coupling at room temperature in plasmonic nanocavities. *Nature* **535**, 127-130 (2016).
- 40 Wang, P., Krasavin, A. V., Nasir, M. E., Dickson, W. & Zayats, A. V. Reactive tunnel junctions in electrically driven plasmonic nanorod metamaterials. *Nat. Nanotechnol.* **13**, 159-164 (2018).

- 41 Li, C. Y. *et al.* Observation of inhomogeneous plasmonic field distribution in a nanocavity. *Nat Nanotechnol* (2020).
- 42 Hyun, J. K. & Lauhon, L. J. Spatially resolved plasmonically enhanced photocurrent from Au nanoparticles on a Si nanowire. *Nano Lett.* **11**, 2731-2734 (2011).
- 43 Mann, S. A. *et al.* Quantifying losses and thermodynamic limits in nanophotonic solar cells. *Nat. Nanotechnol.* **11**, 1071-1075 (2016).
- 44 Reuter, C. *et al.* A versatile scanning photocurrent mapping system to characterize optoelectronic devices based on 2D materials. *Small Methods* **1**, 1700119 (2017).
- 45 Zheng, B. Y. *et al.* Distinguishing between plasmon-induced and photoexcited carriers in a device geometry. *Nat. Commun.* **6**, 7797-7797 (2015).
- 46 Tagliabue, G. *et al.* Quantifying the role of surface plasmon excitation and hot carrier transport in plasmonic devices. *Nat. Commun.* **9**, 3394 (2018).
- 47 Su, D., Zhao, N., Wang, S. J., Zhou, H. L. & Zhang, T. Lysine assisted self-assembly of silica microspheres on textured polycrystalline silicon solar cells for light trapping. in *2019 Photonics & Electromagnetics Research Symposium - Spring (PIERS-Spring)*.
- 48 Ha, D. H., Gong, C., Leite, M. S. & Munday, J. N. Demonstration of resonance coupling in scalable dielectric microresonator coatings for photovoltaics. *ACS Appl. Mater. Interfaces* **8**, 24536-24542 (2016).
- 49 Wu, K., Chen, J., McBride, J. R. & Lian, T. J. S. Efficient hot-electron transfer by a plasmon-induced interfacial charge-transfer transition. *Science* **349**, 632-635 (2015).
- 50 Tan, S. J. *et al.* Plasmonic coupling at a metal/semiconductor interface. *Nat. Photonics* **11**, 806-812 (2017).
- 51 Raj, S., Rai, P. & Yu, Y. T. J. M. L. Pulse electrophoresis deposition of Ag@SiO<sub>2</sub> core-shell nanoparticles on FTO substrate. *Mater. Lett.* **117**, 116-119 (2014).
- 52 Rakic, A. D., Djuricic, A. B., Elazar, J. M. & Majewski, M. L. Optical properties of metallic films for vertical-cavity optoelectronic devices. *Appl. Opt.* **37**, 5271-5283 (1998).
- 53 Palik & Edward, D. *Handbook of optical constants of solids*. (Academic Press, 1985).
- 54 Bour, D. P., Shealy, J. R., Wicks, G. W. & Schaff, W. J. J. A. P. L. Optical properties of Al<sub>x</sub>In<sub>1-x</sub>P grown by organometallic vapor phase epitaxy. *Appl. Phys. Lett.* **50**, 615-617 (1987).
- 55 Adachi, S. J. J. o. A. P. Optical dispersion relations for GaP, GaAs, GaSb, InP, InAs, InSb, Al<sub>x</sub>Ga<sub>1-x</sub>As, and In<sub>1-x</sub>Ga<sub>x</sub>As<sub>y</sub>P<sub>1-y</sub>. *J. Appl. Phys.* **66**, 6030-6040 (1989).
- 56 Schubert, M. *et al.* Optical constants of Ga<sub>x</sub>In<sub>1-x</sub>P lattice matched to GaAs. *J. Appl. Phys.* **77**, 3416-3419 (1995).
- 57 Li, X. *et al.* Multi-dimensional modeling of solar cells with electromagnetic and carrier transport calculations. *Prog. Photovoltaics* **21**, 109-120 (2013).

## Acknowledgments

This work is supported by MOST under Grant Number 2017YFA0205800, NSFC under grant numbers 61875241, 11734005. We thank Qian Fang for SI movie production.

## Author contributions

T. Z. conceived the concepts for the research project. D.S. performed the material synthesis, simulation, micro-region testing and data analysis. X-Y.Z. designed the experiment process and the micro-testing system. L. L. and H-L.Z constructed the micro-region optical path. S-J.W. and Y.Y. performed SEM and EDS tests. N. Z. participated in electronic test system construction. J.Y. W. participated in the discussion of the experiment and the manuscript. D.S. and X-Y. Z. drafted the manuscript.

### **Competing interests**

The authors declare no competing financial interests.

### **Additional information**

**Supplementary information** is available for this paper.

**Correspondence** and requests for materials should be addressed to T.Z.

## Figures

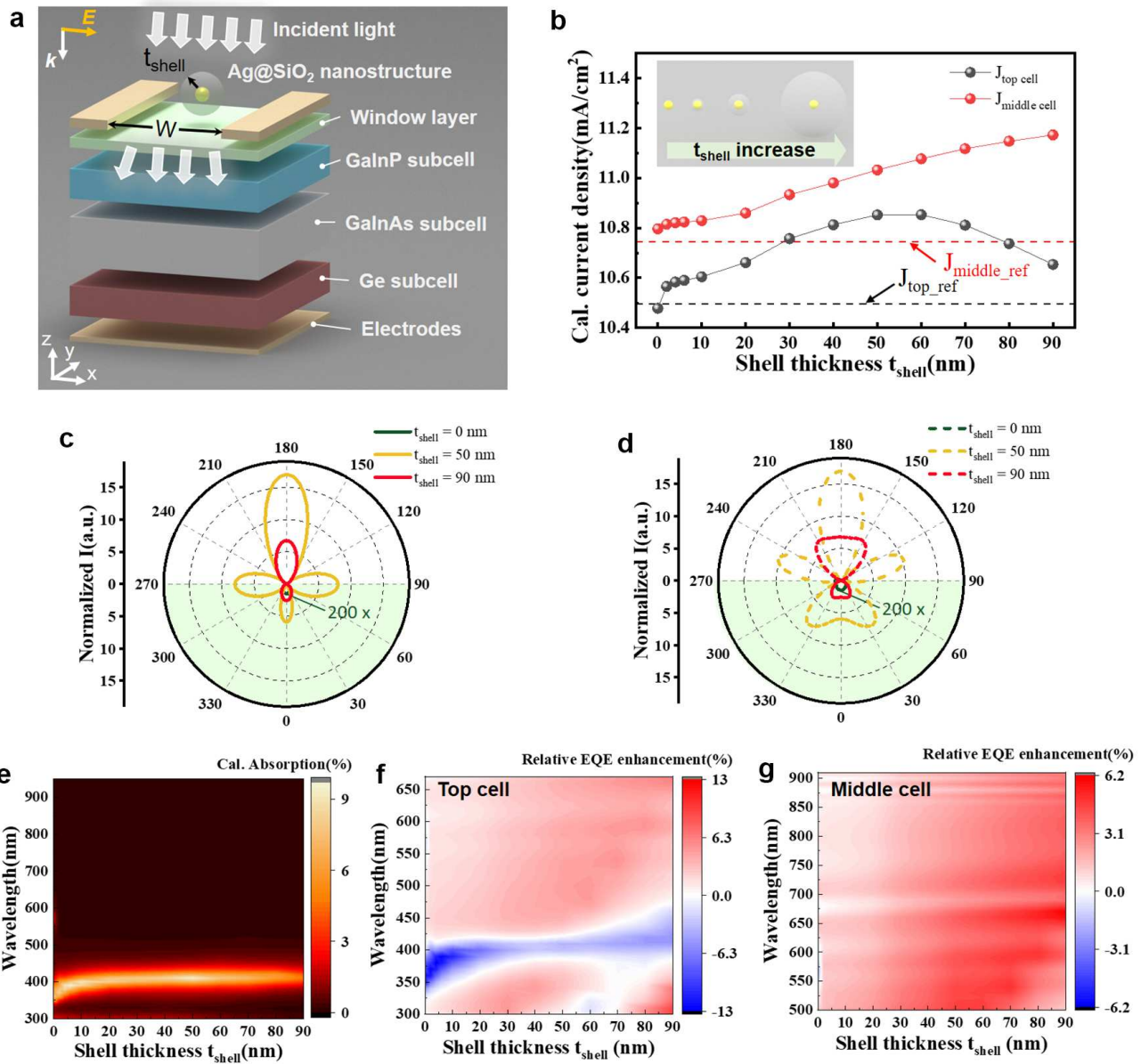


**Figure 1**

Plasmonic enhancement by Ag@SiO<sub>2</sub> nanostructures on MJSCs. a Schematic structure of Ag@SiO<sub>2</sub> atop a GaInP-GaInAs-Ge MJSC. b Calculated current density of top and middle solar cell with different t<sub>shell</sub>. Calculated normalized scattering intensity patterns for the scattering planes parallel (c) and perpendicular (d) to the polarization of the incident wave ( $\lambda=410$  nm). e Calculated Ag@SiO<sub>2</sub> absorption under different t<sub>shell</sub>. Calculated relative EQE enhancement of top (f) and middle (g) cell under different t<sub>shell</sub>.

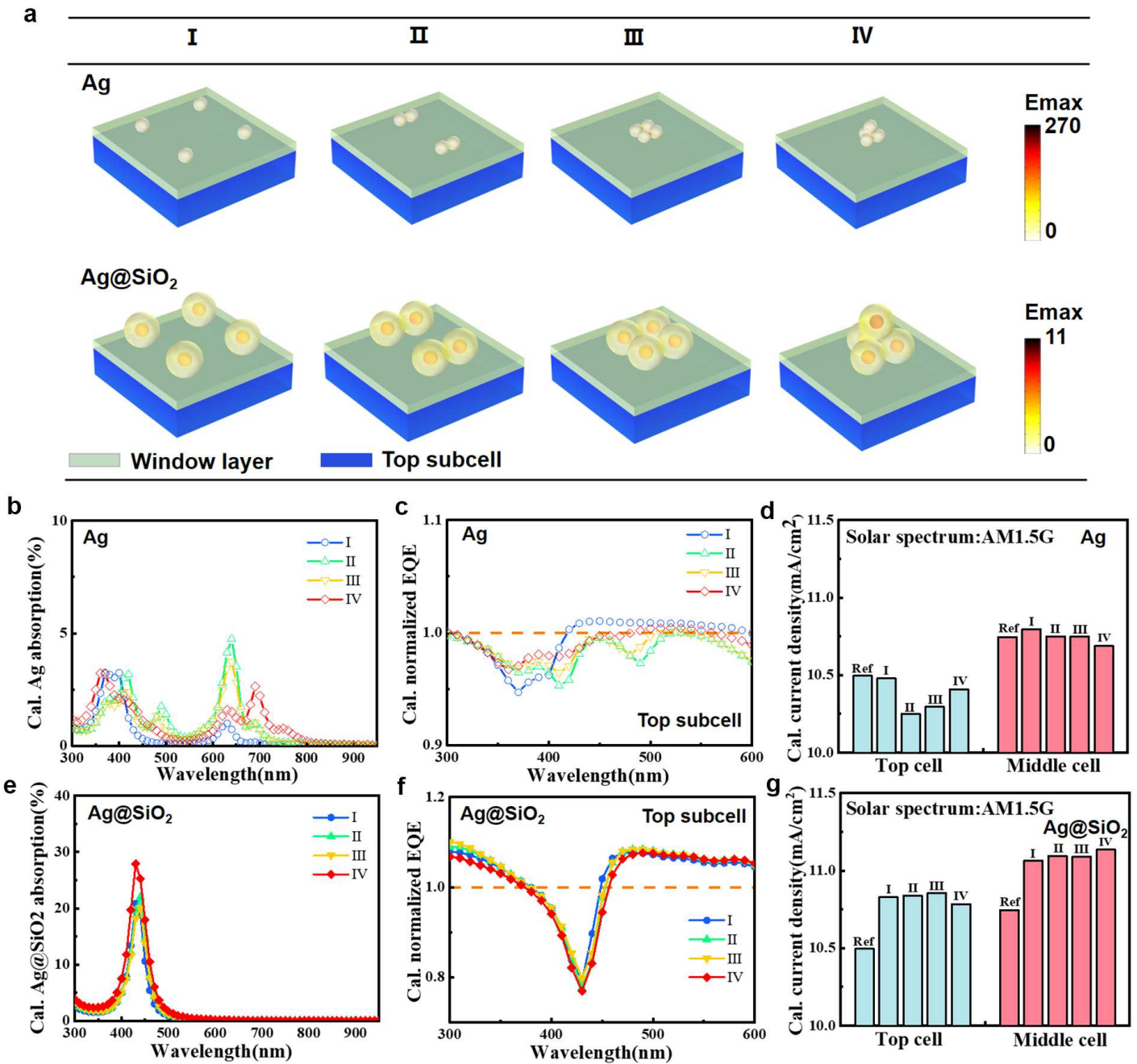


**Figure 2**

3D FEM simulation of different types of aggregates atop of InGaP-GaAs-Ge MJSCs. a Illustrations of different type aggregates and the electrical field distribution in Ag (at 640 nm) and Ag@SiO<sub>2</sub> (at 410 nm) nanostructures. b Calculated Ag absorption. c Calculated normalized EQE of top subcell with Ag nanostructures. d Calculated J<sub>sc</sub> of top subcell and middle subcell with Ag nanostructures. e Calculated Ag@SiO<sub>2</sub> absorption. f Calculated normalized EQE of top subcell with Ag@SiO<sub>2</sub> nanostructures. g Calculated current densities of top subcell and middle subcell with Ag@SiO<sub>2</sub> nanostructures.

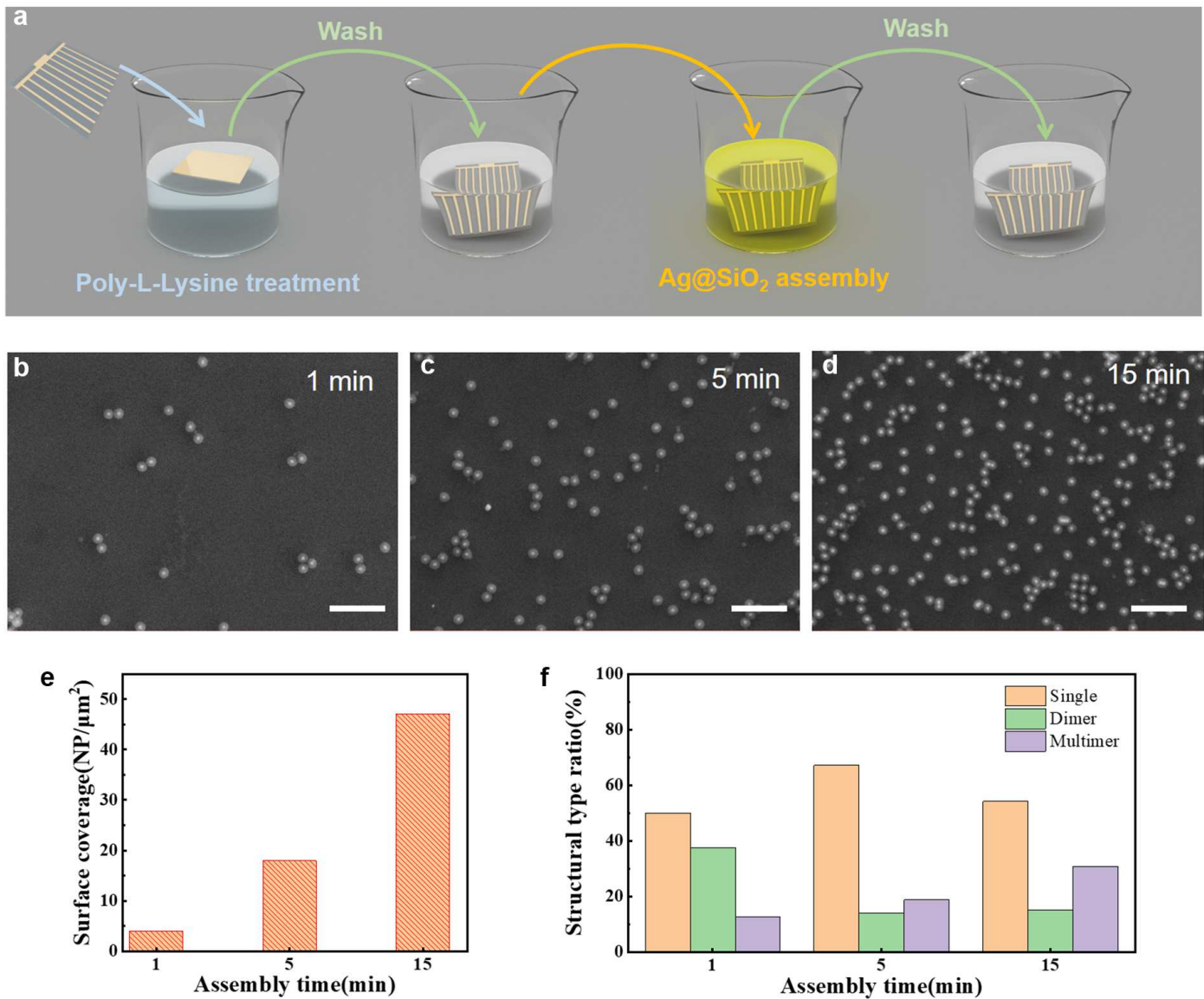


**Figure 3**

SEM analysis of Ag@SiO<sub>2</sub> core-shell nanocoatings. SEM image of different self-assembly time 1 min(b), 5 min(c), and 15 min(d). e Surface coverage analysis of the self-assembly nanocoating under different times. f Structural type analysis of the Ag@SiO<sub>2</sub> nanostructures in the self-assembly nanocoating.

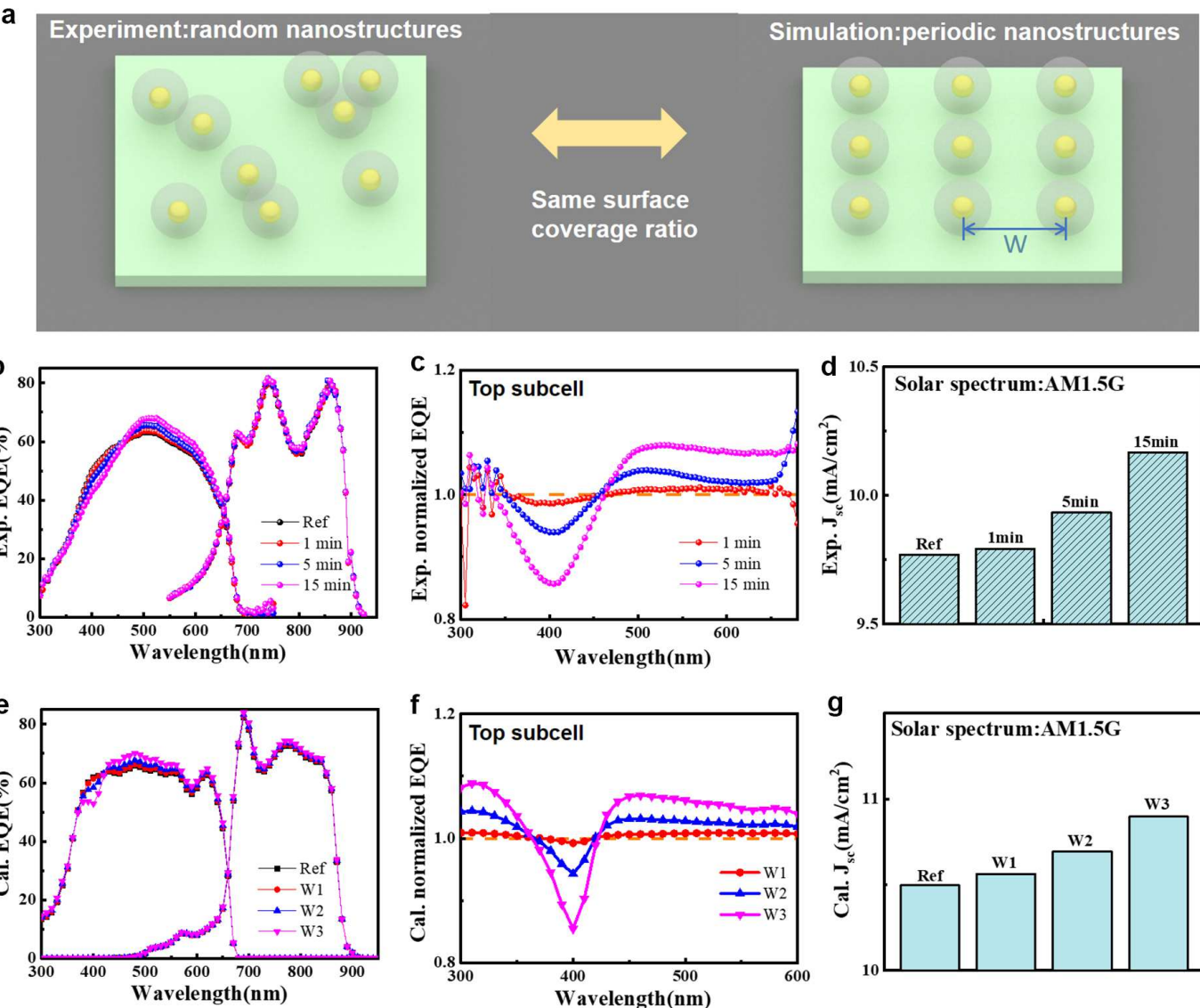


**Figure 4**

Macro enhancement comparison between experimental random distributed and simulational periodic nanostructures. a Schematic of experimental and simulational structure on MJSCs. Experimental EQE (b), normalized EQE of the top cell (c), and  $J_{sc}$  derived from EQE data (d). Simulational EQE (e), normalized EQE of the top cell (f), and  $J_{sc}$  derived from calculated EQE data (g).

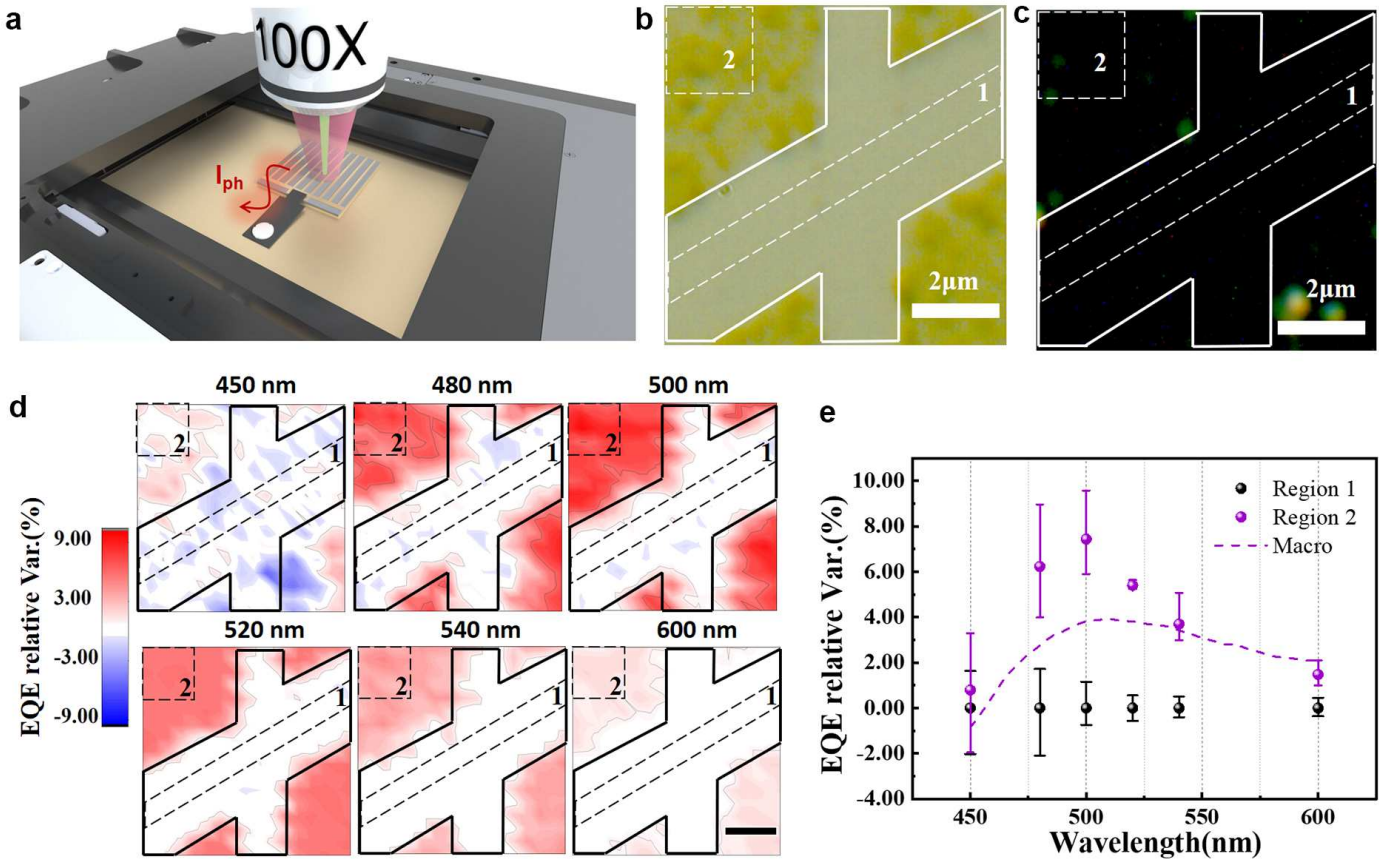


**Figure 5**

Micro-region SPM study for InGaP-GaAs-Ge MJSCs with the Ag@SiO<sub>2</sub> core-shell nanocoating (assembly time, 5 min). a Schematic graph of the submicrometer-scale photoelectrical response measurement for MJSCs. The brightfield (c) and darkfield images (d) of the MJSCs with partly-removed Ag@SiO<sub>2</sub> core-shell nanocoating (assembly time, 5 min). The Ag@SiO<sub>2</sub> nanostructures in the region surrounded by the white frame lines were wiped out. d The wavelength-dependent EQE relative variation images of the same region as the optical images shown in a-b. e EQE relative variation analysis of the background (region 1) and the Ag@SiO<sub>2</sub> core-shell nanocoating (region 2) under the excitation of different wavelengths. The dashed line presents the top subcell's macro normalized EQE curve with an assembly time of 5 min. The error bars show the absolute variations in the specific region.

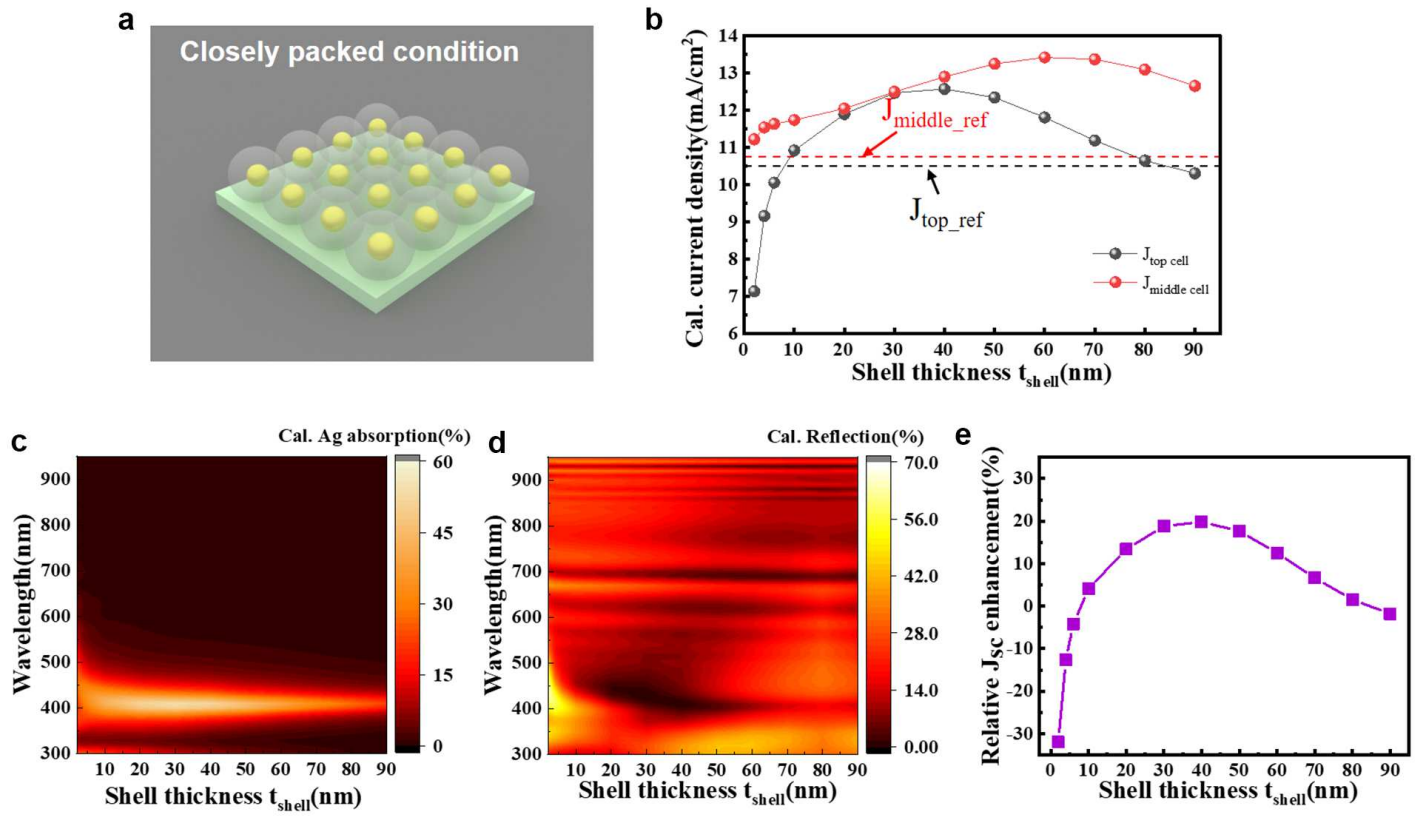


**Figure 6**

Simulation of closely packed Ag@SiO<sub>2</sub> nanostructure array atop the MJSC. a Schematic of the MJSC with closely packed Ag@SiO<sub>2</sub> nanostructures. b Calculated Shell thickness-dependent current density of top and middle solar cell; the dashed line shows the current density without nanostructure. c-d Calculated Ag absorption and reflection of the MJSC with different shell thicknesses. e Relative J<sub>sc</sub> enhancement of the MJSC with closely packed Ag@SiO<sub>2</sub> nanostructure array.

## Supplementary Files

This is a list of supplementary files associated with this preprint. Click to download.

- [SupplementaryMovie1375nm\\_scatteringpattern.mp4](#)
- [SupplementaryMovie2410nm\\_scatteringpattern.mp4](#)
- [SupplementaryMovie3450nm\\_scatteringpattern.mp4](#)
- [Supplementaryinformation.docx](#)